POLITECNICO DI TORINO
Repository ISTITUZIONALE

Effect of electroslag remelting on the VHCF response of an AISI H13 steel

Terms of use:

(Article begins on next page)

19 April 2024

Effect of Electroslag Remelting on the VHCF response of an AISI H13 steel

Author:

A. Tridello[a], D.S. Paolino[b], G. Chiandussi[c], M. Rossetto[d]

[a] Department of Mechanical and Aerospace Engineering, Politecnico di Torino, 10129 Turin, Italy, andrea.tridello@polito.it

b Department of Mechanical and Aerospace Engineering, Politecnico di Torino, 10129 Turin, Italy, davide.paolino@polito.it

[c] Department of Mechanical and Aerospace Engineering, Politecnico di Torino, 10129 Turin, Italy, giorgio.chiandussi@polito.it

[d] Department of Mechanical and Aerospace Engineering, Politecnico di Torino, 10129 Turin, Italy, massimo.rossetto@polito.it

Corresponding Author:

A. Tridello

E-mail address: andrea.tridello@polito.it

Full postal address:

C.so Duca degli Abruzzi 24,

Department of Mechanical and Aerospace Engineering – Politecnico di Torino,

10129 – Turin,

ITALY

Phone number: +39.011.090.6913

Fax number: +39.011.090.6999

Abstract:

Experimental results have shown that high-strength steels can fail in the Very-High-Cycle Fatigue (VHCF) regime with cracks originating from internal defects. Material cleanliness thus plays a major role in the VHCF response of high-strength steels and refinement processes (e.g., Electroslag Remelting (ESR), Vacuum Arc Remelting and Vacuum Induction Melting) could significantly enhance their performance.

The present paper aims at investigating the effect of the Electroslag Remelting (ESR) process on the VHCF behavior of an AISI H13 steel by carrying out fully reversed ultrasonic tension-compression tests on hourglass specimens manufactured with and without the ESR process. Size-effect is also taken into account in the paper: the effectiveness in the prediction of the VHCF response of specimens with large risk-volumes from experimental data on specimens with small risk-volumes is discussed and experimentally validated.

Nomenclature

ESR: ElectroSlag Remelting

σ_u: ultimate strength

HV: Vickers Hardness

E_d: Dynamic Young's modulus

FEA: Finite Element Analysis

V_{90}: 90% risk-volume

$V_{90\%,comp}$: component volume

K_t: stress concentration factor

σ_{nom}: stress amplitude at specimen mid-section

N_f: number of cycles to failure

σ_{local}: stress amplitude at inclusion location

ODA: Optically Dark Area

$\sqrt{a_{d,0}}$: square root of the projected area of the inclusion

LEVD: Largest Extreme Value Distribution

$F_{\sqrt{A_{d,0}}}$: cumulative distribution function of the LEVD

Δk_{th}: threshold stress intensity factor

$\sqrt{a_{ODA}}$: square root of the projected area of the ODA

c_{th}, α_{th}: constant coefficients

X_l: logarithm of the fatigue limit (random variable)

$F_{X_l}(x_l)$: cumulative distribution function of X_l

$X_l|\sqrt{a_{d,0}}$: X_l for a given inclusion size (random variable)

$F_{X_l|\sqrt{a_{d,0}}}(x_l, \sqrt{a_{d,0}})$: cumulative distribution function of $X_l|\sqrt{a_{d,0}}$

σ_{max}: maximum stress in the component

$\sigma_{l,V_{com}}$: maximum allowable stress

1. INTRODUCTION

In recent years, the interest towards the Very-High-Cycle Fatigue (VHCF) behavior of metallic materials has continuously increased[1-3]. The expected fatigue life of components is significantly larger than in the past[1,4-6] and the introduction of new design methodologies against VHCF has become a priority for researchers and industries.

A particular attention in the VHCF literature is devoted to high-strength steels, for their wide usage in critical structural components. High-strength steels exhibit unexpected failures at stress amplitudes below the conventional fatigue limit[7-9], with cracks nucleating from internal defects that formed during the manufacturing process. It is well-known[10] that defect size strongly affects the VHCF response of high-strength steels and a high steel cleanliness is therefore required for critical applications.

In order to reduce the defect content (size and quantity) in steel, different refinement processes are commonly employed: Electroslag Remelting (ESR), Vacuum Arc Remelting and Vacuum Induction Melting are largely employed even if they induce a non-negligible increment of manufacturing costs. VHCF researchers and industries are therefore interested to experimentally verify if the increment of manufacturing costs brings along a significant enhancement of the VHCF response, especially for high-strength steels used in critical applications.

The present paper aims at assessing the influence of the ESR process on the VHCF response of an AISI H13 steel. Fully reversed tension-compression tests are carried out on hourglass specimens with a small risk-volume[11,12] by using the ultrasonic testing machines developed at Politecnico di Torino. In order to highlight the effect of the ESR process, VHCF limits and Probabilistic-S-N (P-S-N) curves are estimated and compared according to the model proposed in Ref.[13]. A general model for the prediction of the VHCF limit at large risk-volumes is also proposed. Experimental results reported in the literature[13,14] for specimens made of the same material but with larger risk-volumes are used for the experimental validation. The effectiveness in the prediction of the VHCF response of large risk-volumes from experimental data on small risk-volumes is discussed and a design methodology is finally proposed.

2. MATERIALS AND EXPERIMENTAL TESTS

Ultrasonic VHCF tests are carried out on an AISI H13 steel obtained by conventional casting (denoted as H13 in the following) and on an AISI H13 obtained by conventional casting and refined with an ESR process (denoted as H13-ESR in the following). In Section 2.1, the material properties and the ESR process are described. In Section 2.2, the geometry of the hourglass specimens is reported and details on the heat treatment are provided. In Section 2.3, the mechanical properties of the investigated H13 steels are compared. Finally, the testing configuration is described in Section 2.4.

2.1 Materials

The AISI H13 (EN 40CrMOV5-1 steel, according to UNI EN ISO 4957) is classified as an hot work tool steel, but it is also employed in critical applications where resistance to VHCF failures is required (e.g., fuel injectors for naval engines and aerospace components). The H13 and the H13-ESR are provided in the annealed condition by the Böhler Uddeholm: their chemical composition is reported in Table 1.

Table 1: Chemical composition of the AISI H13 steel.

Element	C	Si	Mn	Cr	Mo	V
%	0.39	1	0.4	0.4	5.3	0.9

Both steels are obtained by conventional casting. After the production process, the H13-ESR is also subjected to ESR, which involves a second remelting and a subsequent fine solidification. The entire ESR process is performed in a protective atmosphere in order to limit the hydrogen absorption[15] and to further enhance the steel cleanliness. Through the ESR process, large defects, micro and macro segregation and non-metallic inclusions are removed and the sulphur content is significantly reduced[16,17] . The refinement process increases the manufacturing cost by about the 13%.

2.2 Specimen geometry and heat treatment

Hourglass specimens are used for the experimental tests. The specimen geometry is analytically designed and then verified through a Finite Element Analysis (FEA). The stress intensity factor, k_t (Ref.[12]), is smaller than 1.07. The specimen risk-volume V_{90}, defined as the volume of material subjected to a stress amplitude above the 90% of the maximum applied stress[10-12], is equal to 194 mm^3. Fig. 1 shows the geometry of the hourglass specimen used for the experimental tests.
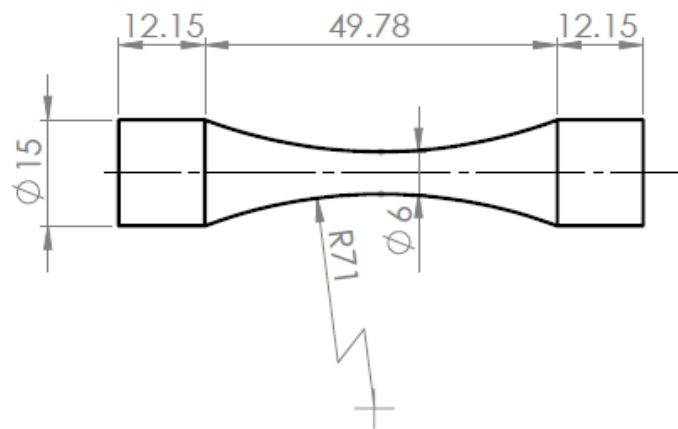

Figure 1: Geometry of the hourglass specimen.

The specimen shape is obtained through a CNC machining process starting from rectangular bars with dimensions $32 \times 32 \times 115 \text{ mm}$. After the production process, hourglass specimens are quenched and tempered in an ordinary industrial cycle. The heat treatment involves preheating at 1023 K, austenitizing at 1030 K, gas quenching and triple tempering (first tempering at 793 K, second and third tempering at 813 K). A homogeneous tempered martensite microstructure, shown in Fig. 2, is obtained after the heat treatment.
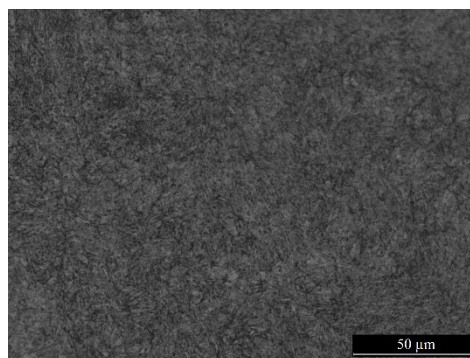

Figure 2: Tempered martensite microstructure obtained after the heat treatment (H13-ESR steel).

Finally, specimens are fine polished with sand papers with increasing grit from #200 to #1200.

2.3 Preliminary mechanical characterization

Two H13 specimens and two H13-ESR specimens are tensile tested up to failure to assess the ultimate strength, σ_u.

The Vickers hardness, HV, is experimentally assessed according to Ref.[18]. The resulting HV is the average value of three repeatable measurements made at different locations on the specimen cross-section.

The dynamic Young's modulus is experimentally measured through the Impulse Excitation Technique (IET). Two rectangular bars of the investigated materials are designed according to Ref.[19]. The first longitudinal mode is used for the computation of the dynamic Young's modulus, E_d.

Table 2 reports the measured mechanical properties for the two investigated steels. Due to the limited scatter of the experimental results, only the average values of the measurements are reported.

Table 2: Mechanical properties of the investigated steels.

Material	σ_u [MPa]	E_d [GPa]	HV [HV]
H13	2000	212	560
H13-ESR	2100	213	560

According to Table 2, the mechanical properties of the two investigated steels are not significantly influenced by the ESR process: the HV does not change and the dynamic Young's modulus and the tensile strength are only slightly incremented after the ESR process.

2.4 VHCF tests

Experimental tests are performed by using two ultrasonic testing machines developed at Politecnico di Torino. Fully reversed tension-compression tests are performed at a load frequency of $20\,\text{kHz}$.

The displacement at the specimen free end, measured with a laser displacement sensor, is kept constant during the test through a closed loop control. Therefore, by assuming a macroscopic linear elastic behavior of the tested material, the stress amplitude in the specimen mid-section is kept constant during the test. The correlation between the displacement amplitude at the specimen free end and the stress at the specimen center is determined through an accurate strain gage calibration.

The specimen temperature is continuously monitored during the test by using an infrared sensor. Intermittent tests[2,3] are carried out in order to limit the specimen self-heating due to internal damping[20]. The specimen temperature is maintained between $298\,\text{K}$ and $303\,\text{K}$. Vortex tubes are employed to limit the temperature increment and to speed up the specimen cooling. The actual frequency of the test (frequency evaluated by taking into account the pause phase) is larger than $15\,\text{kHz}$ for each test. The temperature distribution within the risk-volume is verified to be uniform through FEA, with a variation smaller than 1%. Fig. 3 shows the measuring system (laser displacement sensor and infrared sensor) and the vortex tubes in a typical configuration during the ultrasonic VHCF test.

Figure 3: Typical setup in an ultrasonic VHCF test.

3. EXPERIMENTAL RESULTS

The experimental results are summarized in Section 3.1. Fracture surfaces, observed by using the optical microscope and the Scanning Electron Microscope (SEM), are analyzed in Section 3.2. Finally, in Section 3.3, the statistical distributions of the defect size for the two investigated steels are estimated and compared.

3.1 S-N plot

Ultrasonic VHCF tests are performed up to failure or up to 10^{10} cycles (runout). Table 3 summarizes the experimental data. The number of tested specimens, the nominal applied stress range, σ_{nom} (applied stress at specimen mid-section), the number of runouts and the number of cycles to failure, N_f (minimum and maximum value), are reported in the table.

Table 3: Summary of the experimental results.

Material	Number of specimens	Stress range [MPa]	Number of runouts	Minimum N_f	Maximum N_f
H13	15	$[570 - 710]$	3	$4.5 \cdot 10^6$	$9.4 \cdot 10^9$
H13-ESR	16	$[630 - 810]$	3	$2.0 \cdot 10^7$	$3.5 \cdot 10^9$

In order to determine the crack origin, fracture surfaces are observed with an optical microscope and a Scanning Electron Microscope (SEM). All the fatigue failures originated from inclusions inside the risk-volume.

Failure locations are also analyzed: the radial location is assessed through an accurate image processing of the fractographs, whereas the axial location is measured by using a digital caliber with resolution 0.01 mm. Fig. 4 shows the distribution of failures within the specimen risk-volume. The abscissa axis reports the location of the failures in the axial direction z (normalized with respect to the maximum distance of a failure from the specimen center, $L_{max,f}$); whereas, the ordinate axis reports the position of the failures in the radial direction r_f (normalized with respect to the specimen radius at the corresponding axial location, r).
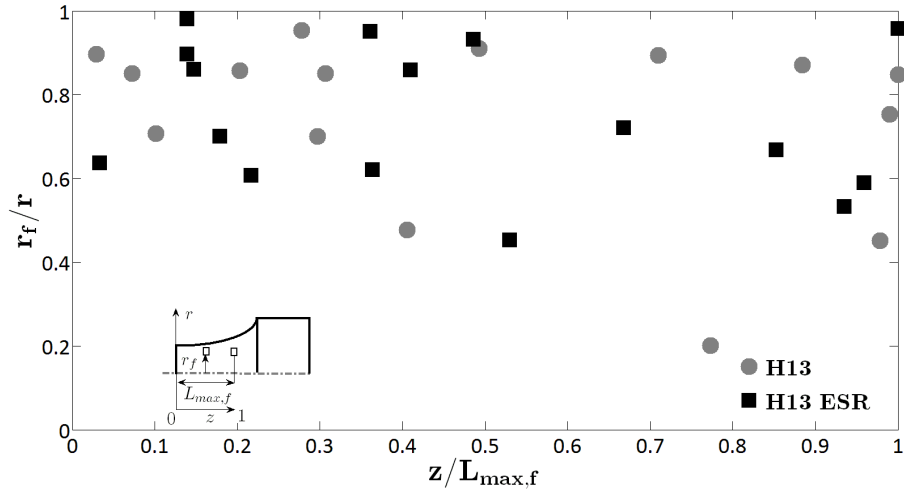
Figure 4: Distribution of failures within the specimen risk-volume: failure location in the radial direction vs. failure location in the axial direction.

According to Fig. 4, fatigue failures are randomly distributed within the specimen risk-volume: the uniformity of the Vickers hardness after the heat treatment and the limited temperature variation along the specimen cross-section did not affect the VHCF test. All failures are included within V_{90}: according to Ref.[10,11], V_{90} can be conservatively considered as the critical volume in which fatigue failures can occur. In order to take into account the stress variation within the specimen risk-volume, the stress amplitude at the inclusion location (local stress amplitude, σ_{local}) is considered in the following for the analysis of the experimental data. Fig. 5 shows the S-N plot of the experimental results, computed by considering the local stress amplitude.
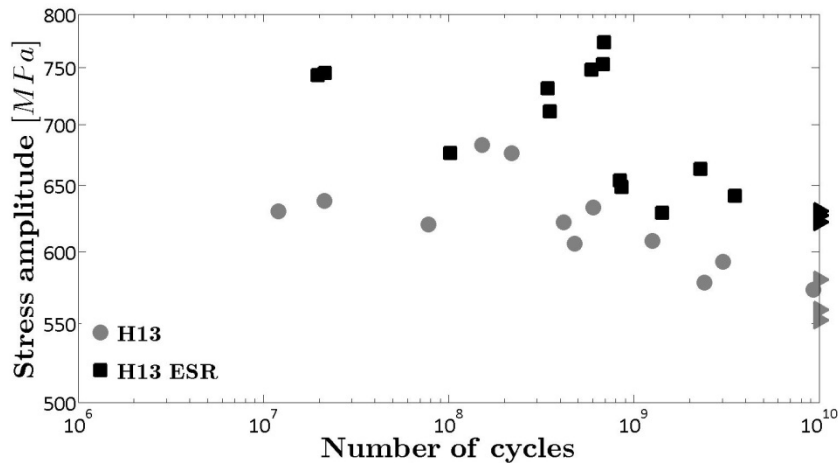

Figure 5: S-N plot of the experimental results computed by considering the local stress amplitude, σ_{local}.

According to Fig. 5, failure data for H13-ESR are above those for H13: H13-ESR runouts occur at about 620 MPa; whereas H13 runouts occur at stress amplitudes smaller than 580 MPa. Runouts in tests on Gaussian specimens[13,14] with $V_{90} = 2300 \text{ mm}^3$ occurred at smaller stress amplitude (473 MPa for the H13 and at 570 MPa for the H13-ESR). VHCF decrement due to size-effect and its implication on design methodologies will be discussed in Section 4.4.

3.2 Inclusion analysis

All fracture surfaces show a fish-eye morphology, with an inclusion at the center of the Optically Dark Area (ODA, according to Ref.[10]) Fig. 6a shows a typical fish-eye fracture; Fig. 6b shows an enlargement of the ODA.

(a)   (b)

Figure 6: Fish-eye fracture found experimentally: a) fish-eye morphology; b) enlargement of the ODA.

Energy Dispersive X-ray analyses are carried out to assess the chemical composition of the inclusions originating failure. Non-metallic oxide type inclusions with large percentages of Aluminum, Calcium and Manganese are found at the origin of the fatigue failures in all the tested specimens. 33 out of 34 inclusions show a spherical shape: in one case, a cluster of small inclusions is at the origin of the fatigue failure (H13-ESR). Accordingly, it can be concluded that spherical oxide-type inclusions are the critical defects even after the ESR process. Fig. 7a shows an example of a spherical inclusion; Fig. 7b shows the unique case of cluster of small inclusions.

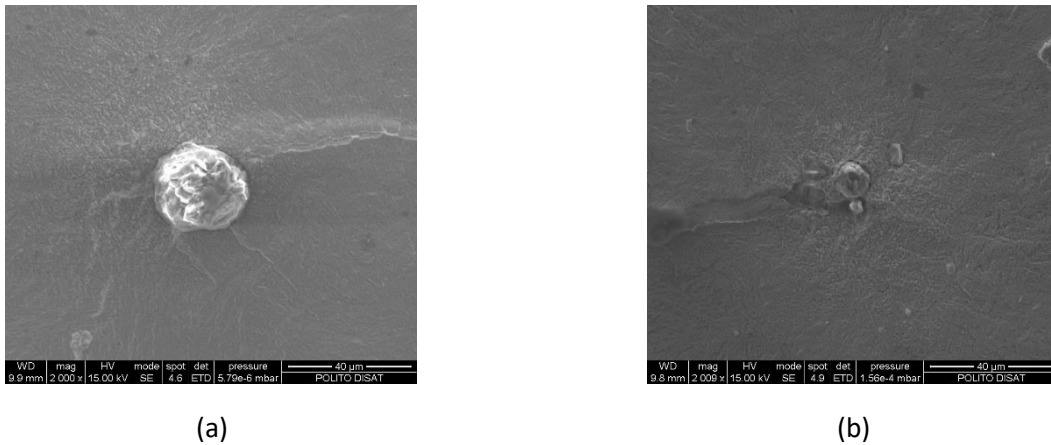(a)   (b)

Figure 7: Different types of initial defect: (a) single spherical inclusion (H13; $\sigma_{local} = 608$ MPa; $N_f = 1.25 \cdot 10^9$); (b) cluster of small inclusions (H13-ESR; $\sigma_{local} = 629$ MPa; $N_f = 1.42 \cdot 10^9$).

3.3 Statistical distribution of the inclusion size

The inclusion size plays an important role in the mechanism of crack initiation in high-strength steels and therefore it significantly affects the VHCF response[10]. According to Ref.[10,21], the defect at the origin of the fatigue crack is the largest inside the risk-volume and, therefore, its size follows the Largest Extreme Value distribution (LEVD). Following a common procedure adopted in the VHCF literature[22], runouts are tested at a higher stress amplitude (increased by 30 MPa) in order to induce an internal failure and to reveal the largest inclusion inside the risk-volume. Fig. 8 shows the Gumbel plot of the inclusion sizes. Parameter estimation is carried out according to the Maximum Likelihood Principle.
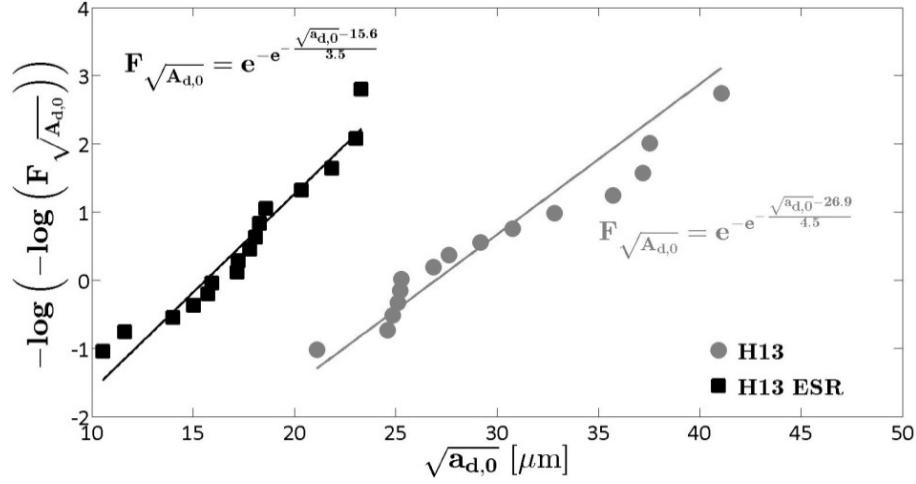
Figure 8: Gumbel plot of the inclusion size for the investigated steels.

As shown in Fig. 8, inclusions are significantly larger in H13: the ESR process effectively removes large and critical inclusions from the steel. The largest inclusion in H13-ESR (23.3 μm) is about half of the largest inclusion in H13 (41.0 μm). Moreover, inclusions in H13-ESR are in a small range $[10-23]$ μm, whereas 14 out of 15 inclusions in H13 are larger than 23 μm and in a larger range $[21-41]$ μm.

By considering the inclusion size obtained by testing larger risk-volumes[13,14], the largest inclusion found experimentally increased to 56 μm for the H13 and to 31 μm for H13-ESR: the increment of the inclusion size due to size-effect is smaller after the refining process.

4. P-S-N CURVES AND SIZE EFFECT

Experimental results are analyzed according to the model proposed in Ref.[13], in order to estimate the VHCF limits and the P-S-N curves. In Section 4.1, the threshold stress intensity factors for the two steels are estimated and compared. The VHCF limits and the P-S-N curves are compared in Section 4.2 and in Section 4.3 respectively, in order to assess the actual influence of the ESR process on the VHCF response. Finally, in Section 4.4, the curves of the VHCF limits as a function of the risk-volume are estimated from the experimental results. The effectiveness in the prediction of the VHCF response at larger risk-volume is also verified and discussed.

4.1 Stress Intensity Factor threshold

The general formulation proposed in Ref.[13] is considered for the threshold Stress Intensity Factor (SIF) threshold, Δk_{th} ($\Delta k_{th} = 10^{-3} c_{th}(HV+120)\sqrt{a_d}^{\alpha_{th}}$, being c_{th}, α_{th} two material constants and a_d the projected area of the defect). The constant coefficients c_{th} and α_{th} are estimated through the least square method, by considering that the SIF evaluated at the border of the ODA must be equal to the Δk_{th} value, according to Ref.[10,13,23]. Fig. 9 plots the Δk_{th} values with respect to $\sqrt{a_{ODA}}$ (a_{ODA} is the projected area of the ODA) in a log-log plot, together with the estimated linear model.

$$k_{th,\alpha} = 1.26 \cdot 10^{-3} \cdot (HV + 120) \cdot \sqrt{a_{ODA}}^{-0.39}$$

$$\mathbf{k_{th,\alpha} = 1.35 \cdot 10^{-3} \cdot (HV + 120) \cdot \sqrt{a_{ODA}}^{-0.38}}$$
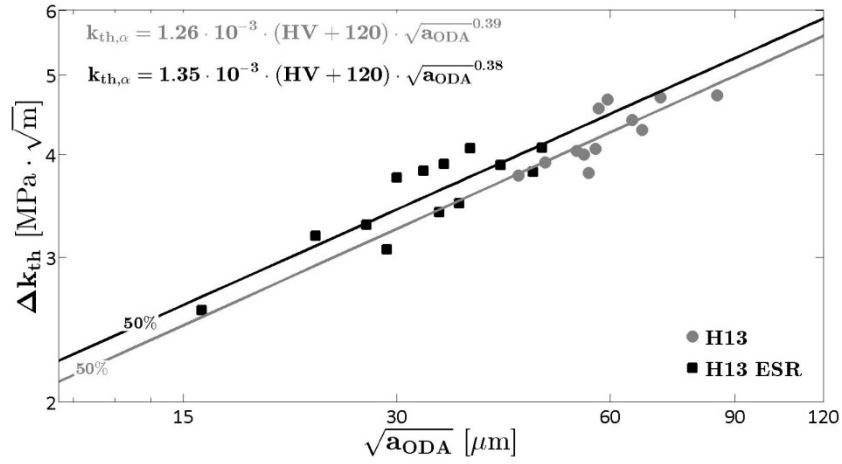
Fig. 9: SIF threshold with respect to $\sqrt{a_{ODA}}$ for the investigated steels.

As shown in Fig. 9, the assumed linear model is in good agreement with the experimental data. The Δk_{th} follows the same linear trend before and after the ESR process, with similar estimated coefficients. The slope of the interpolating function is close to the value reported in the VHCF literature[10,24] ($\alpha_{th} = 1/3$) for high-strength steels with Vickers hardness smaller than 600 HV. Fig. 10 plots the Δk_{th} values with respect to the number of cycles to failure.
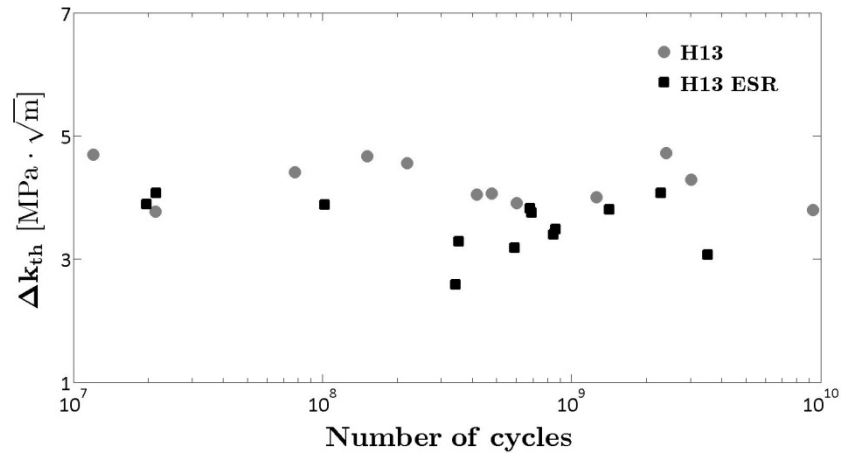
Figure 10: SIF threshold with respect to the number of cycles to failure for the investigated steels.

According to Fig. 10, the Δk_{th} values are included in a small range: 96% of the Δk_{th} values are between $3 \text{ MPa} \cdot \sqrt{m}$ and $5 \text{ MPa} \cdot \sqrt{m}$, which is close to the range found in Ref.[25,26]. In agreement with Ref.[27], the Δk_{th} values are smaller for H13-ESR, due to the smaller ODA size ($[44 - 85]$ μm for H13 and $[19 - 48]$ μm for H13-ESR).

4.2 VHCF limit

The VHCF limit is estimated according to the model proposed in Ref.[13]. Fig. 11 plots the estimated median VHCF limits with respect to the inclusion size, together with the failure data.

$$s_{l,\sqrt{a_{d,0}},\alpha} = \frac{1.25 \cdot (HV + 120)}{\sqrt{a_{d,0}}^{0.11}} \cdot 10^{\Phi^{-1}(\alpha) \cdot 0.03}$$

$$s_{l,\sqrt{a_{d,0}},\alpha} = \frac{1.16 \cdot (HV + 120)}{\sqrt{a_{d,0}}^{0.11}} \cdot 10^{\Phi^{-1}(\alpha) \cdot 0.02}$$
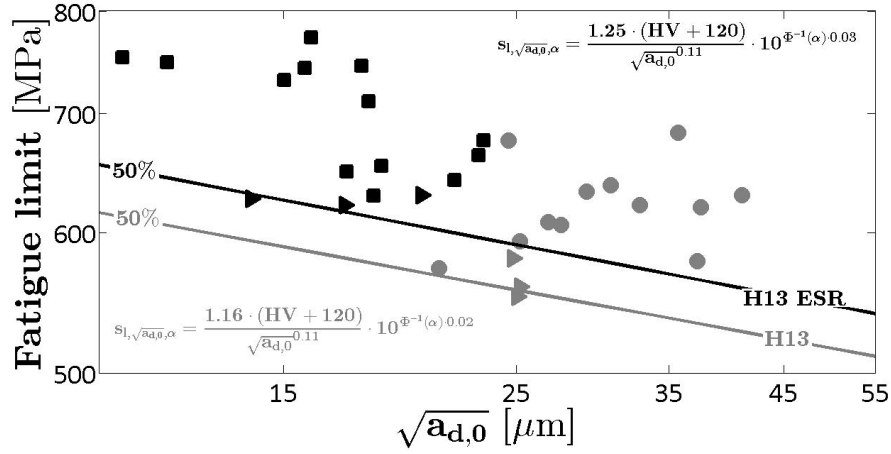
Figure 11: Median fatigue limit curve for the H13 and the H13-ESR steel.

As shown Fig. 11, no failure occurs below the estimated VHCF limit curves, according to the definition of fatigue limit. The H13-ESR curve is always above the H13 curve. By considering the largest inclusion in each steel type, the fatigue limit is 527 MPa ($\sqrt{a_{d,0}} = 41$ μm) for H13, whereas it is 595 MPa ($\sqrt{a_{d,0}} = 23$ μm) for H13-ESR, with a difference larger than 68 MPa (13%).The removal of large inclusions significantly enhances the VHCF response of H13-ESR.

4.3 P-S-N curves

The P-S-N curves are estimated and compared following the methodology reported in Ref.[13]: the fatigue life is considered normally distributed with mean linearly dependent on the applied stress and constant standard deviation. According to Section 4.2 and to Ref.[28], the presence of a fatigue limit is assumed at the end of the P-S-N curves.

Fig. 12 plots, for each steel type, the 0.1-th and the median P-S-N curves corresponding to initial defect with median size.
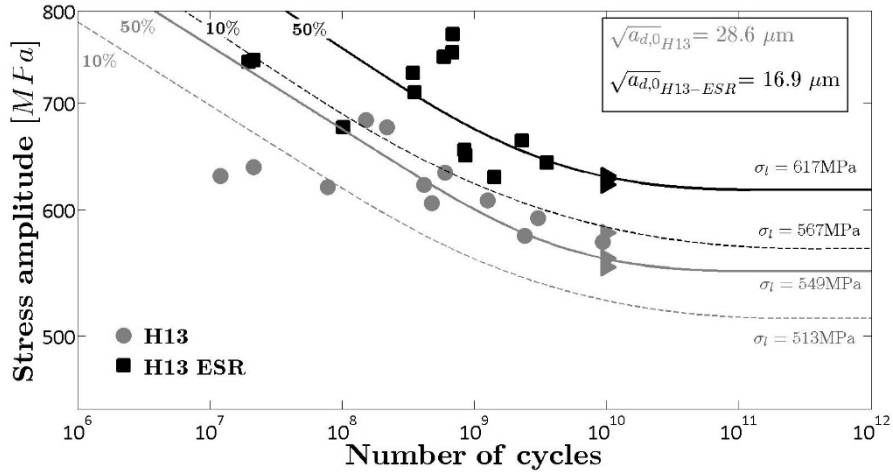

Figure 12: P-S-N curves for an initial defect with median size.

According to Fig. 12, the estimated model is in agreement with the experimental data: about 50% of the failures are above the median P-S-N curves for both steel types. The P-S-N curves show that the enhancement of the VHCF response is almost constant within the VHCF region, with a difference of about 70 MPa (13%). The 0.1-th P-S-N curves are not below all the VHCF failures, due to the large scatter of the defect sizes.

Fig. 13 shows the marginal 0.01-th P-S-N curves[13] for the investigated steels. According to the model in Ref.[8], the marginal P-S-N curves, estimated by considering the inclusion size distribution in Fig. 8, do not depend on the inclusion size.
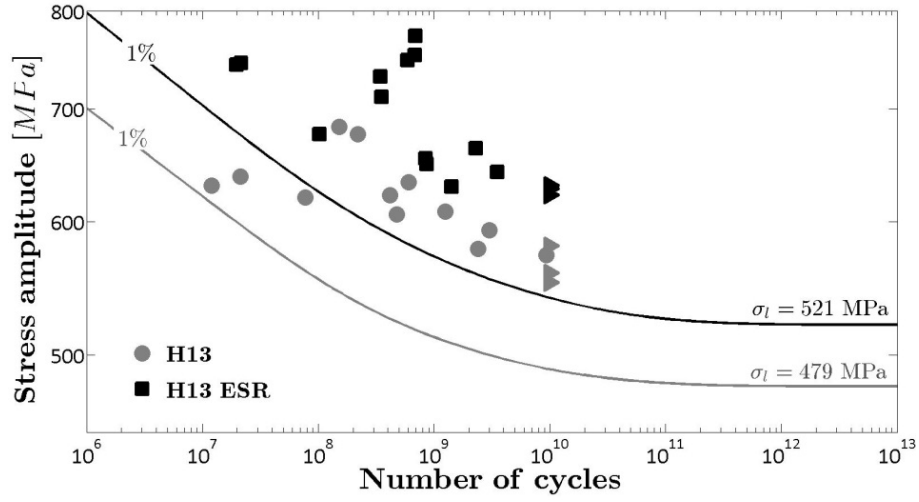

Figure 13: Marginal 1% P-S-N curves for the two investigated steels.

As shown in Fig. 13, the estimated marginal curves are in good agreement with the experimental data: regardless of the inclusion size, no failure occurs below the estimated curves. Therefore, the marginal 1% P-S-N curve can be effectively used as a design curve when designing components against VHCF failure. The H13-ESR curve is always above the H13 curve. The difference is almost constant in the VHCF region, with a difference of about 420 MPa (8%).

It is worth noting that the estimated P-S-N curves refer to the specific investigated risk-volume, which is quite below the typical risk-volumes of structural components subject to VHCF (e.g., high-speed train axles and wheels, turbine blades, rolling bearings, gears). The effectiveness in the prediction of the VHCF response of specimens with large risk-volumes from experimental data on specimens with small risk-volumes is discussed and experimentally validated in the following Section.

4.4 Design methodology

It is well-known in the VHCF literature[10-12,29-31] that size-effect significantly affects the response of high-strength steels: the probability of large critical defects increases as the volume of material increases, with a consequent reduction of the VHCF life and strength. Therefore, size-effect must be taken into account when components are designed: typical investigated risk-volumes (hourglass specimens with V_{90} of about 30 mm^3) are significantly smaller than component risk-volumes (e.g., V_{90} of railway axles is about 100.000 mm^3, according to Ref.[32]) and the VHCF response of components is generally predicted from the experimental results obtained on small specimens.

In the VHCF literature[10,23], design methodologies involve the prediction of the largest inclusion in the component volume through the LEVD and, thereafter, the estimation of the VHCF response from the well-known Murakami's square-root of area formulation. However, a small number of experimental results is available to verify if the predicted and the actual VHCF responses are in good agreement.

In the following, the *fatigue limit design curve* (VHCF limit as a function of the risk-volume) is estimated for the two investigated steels. The VHCF limit predicted at 2300 mm^3 is compared with the VHCF limit reported in Ref.[13,14].

The cumulative distribution function of the logarithm of the VHCF limit $F_{X_l}(x_l)$ for a reference risk-volume $V_{90,ref}$ is expressed by[13]:

$$F_{X_l}(x_l) = \int F_{X_l|\sqrt{a_{d,0}}}(x_l, \sqrt{a_{d,0}}) \cdot F_{\sqrt{A_{d,0}}}(\sqrt{a_{d,0}}) \cdot d\sqrt{a_{d,0}}. \tag{1}$$

where x_l is the logarithm of the VHCF limit, $F_{X_l|\sqrt{a_{d,0}}}$ is the cumulative distribution function of $X_l|\sqrt{a_{d,0}}$ (the logarithm of the VHCF limit for a given initial defect size). By substituting $F_{X_l}(x_l)$ with α, the α-th quantile of the VHCF limit can be obtained by solving Eq. (1) with respect to x_l. The VHCF limit for a different volume V_{90} larger than $V_{90,ref}$ can be obtained by modifying the LEVD function in Eq. (1):

$$F_{X_l}(x_l) = \int F_{X_l|\sqrt{a_{d,0}}}(x_l, \sqrt{a_{d,0}}) \cdot \left(\frac{V_{90}}{V_{90,ref}} \cdot \left[F_{\sqrt{A_{d,0}}} \right]^{\frac{V_{90}}{V_{90,ref}}-1} \right) \cdot d\sqrt{a_{d,0}}. \tag{2}$$

Eq. (2) permits to predict the VHCF limit for a volume V_{90} larger than $V_{90,ref}$ and to estimate the *fatigue limit design curve* at different probabilities.

Fig. 14 shows the median *fatigue limit design curves* for the two investigated steels. The actual median VHCF limits at $V_{90} = 2300 \text{ mm}^3$ reported in Ref.[12,13] are also plotted. In Fig. 14, $\sigma_{l,H}$ is the VHCF limit predicted from tests on hourglass specimens and $\sigma_{l,G}$ is the actual VHCF limit obtained from tests on Gaussian specimens with $V_{90} = 2300 \text{ mm}^3$ (Ref.[12,13]).
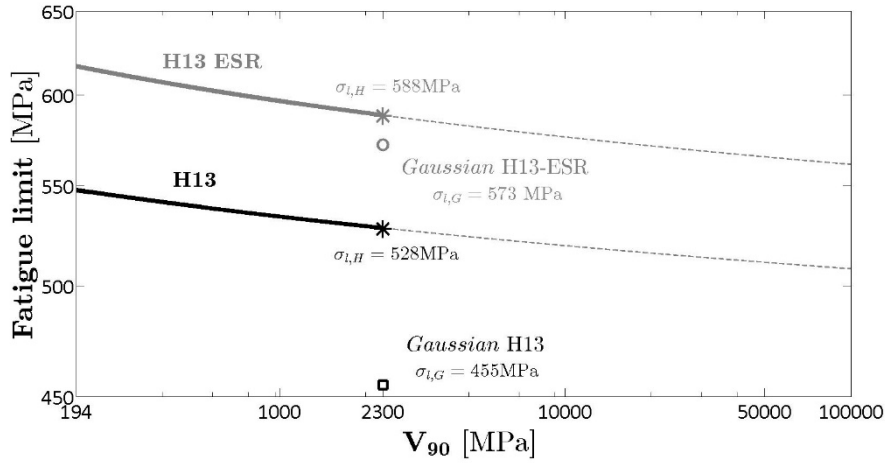

Figure 14: Median fatigue limit design curves for the two investigated steels: $\sigma_{l,H}$ and $\sigma_{l,G}$ denote predicted and experimental[12,13] values at $V_{90} = 2300 \text{ mm}^3$.

According to Fig. 14, the predicted VHCF limits are larger than the experimental values for both steel types. The difference is larger than 16% (73 MPa) for H13, whereas it reduces to 2.6% for H13-ESR (15 MPa). Therefore, even if it is not conservative, a more effective prediction can be obtained with H13-ESR. The difference is due to the different steel cleanliness. For H13, inclusion size is in a larger range that does permit an accurate prediction from the estimated LEVD: the largest inclusion predicted from hourglass specimens (38 µm) is significantly smaller than the actual largest inclusion reported in Ref.[12] (56 µm). Therefore, in case of H13, prediction yields a dangerous non-conservative value.

The *fatigue limit design curve* can be also used as a design curve, according to the procedure shown in Fig. 15.
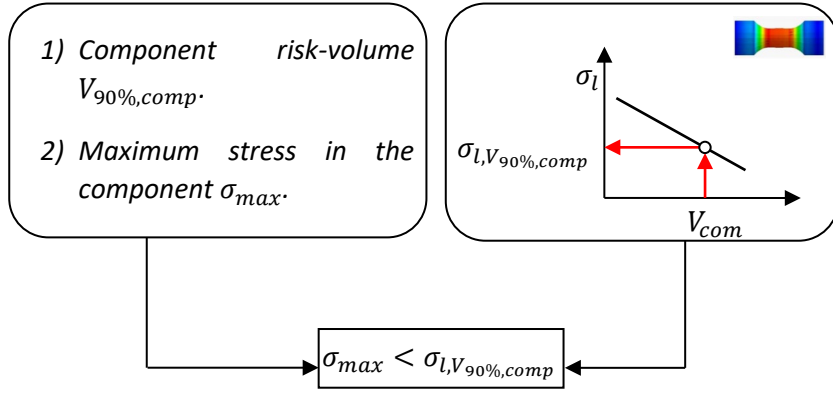
Figure 15: Proposed design methodology based on the *fatigue limit design curve.*

Following the graph in Fig. 15, the maximum stress in the component, σ_{max}, the component risk-volume, $V_{90\%,comp}$, and the fatigue limit design curve are the necessary inputs for the application of the proposed design methodology. $V_{90\%,comp}$ and σ_{max} can be assessed through FEA. The maximum allowable stress for the component, $\sigma_{l,V_{90\%,comp}}$, can be obtained from the *fatigue limit design curve*. The component is verified if the maximum stress in the component is smaller than the predicted $\sigma_{l,V_{90\%,comp}}$.

The proposed design methodology can be easily applied for the design of components subjected to VHCF. However, it can be applied only if the *fatigue limit design curves* are properly estimated and allow for a reliable prediction of the maximum allowable stress.

4. Conclusions

The influence of the ESR process on the VHCF response of an AISI H13 steel was experimentally assessed. Ultrasonic fully reversed tension-compression tests were carried out on hourglass specimens with risk-volume of $194\ mm^3$. The effect of the ESR process was assessed by comparing the inclusion population, the VHCF limit and the P-S-N curves.

Spherical oxide-type inclusions were found at the origin of the fatigue crack in the two investigated H13 steels. However, inclusions were significantly smaller after the ESR process.
The influence of the inclusion content was investigated by comparing the VHCF limits and the P-S-N curves. The VHCF limit corresponding to the largest inclusion in the remelted steel (H13-ESR steel) is about 13% larger than that of the unrefined steel (H13 steel). The P-S-N curves for H13-ESR were above the P-S-N curves for H13: the difference, about 8%, was almost constant in the whole VHCF region. The estimated 0.1% P-S-N curves were below all the experimental failures and therefore could be conservatively used as design curves against VHCF failure. The experimental results confirmed that, together with the enhancement of the steel cleanliness, a significant enhancement of the VHCF response can be obtained through the ESR process.

Size effect was also investigated and discussed. The *fatigue limit design curves* (VHCF limit as a function of the risk-volume) were estimated and used to predict the VHCF limits for specimens with larger risk-volumes, already investigated in the literature. Even if slightly non-conservative, an accurate prediction of the VHCF limit was attained only for H13-ESR; whereas, for H13, the prediction was dangerously non-conservative. The obtained results suggest that predictions of size effects could lead to dangerous non-conservative responses and warn that the non-conservativeness may be larger for high-strength steels with lower cleanliness.

REFERENCES

1 Bathias, C., Paris, P.C. (2005) Gigacycle fatigue in mechanical practice. CRC Dekker, New York, USA.

2 Stanzl-Tschegg, S. (2014) Very high cycle fatigue measuring techniques. *Int. J. Fatigue,* **60**, 2-17.

3 Mayer, H. (2016) Recent developments in ultrasonic fatigue. *Fatigue Fract. Eng. Mater. Struct.,* **39** (issue 1), 3-29.

4 Pyttel, B., Brunner, I., Schwerdt, D., Berger, C. (2012) Influence of defects on fatigue strength and failure mechanisms in the VHCF-region for quenched and tempered steel and nodular cast iron . *Int. J. Fatigue,* **41**, 107-118.

5 Bacher-Hoechst, M., Issler, S. (2013) Assessment of Very High Cycle Fatigue (VHCF) Effects in Practical Applications . *Procedia Eng,* **66**, 26-33.

6 Shanyavskiy A. (2014), Very-High-Cycle-Fatigue of in-service air-engine blades, compressor and turbine. *Sci China Press*, 57, 19-29.

7 Bathias, C. (1999) There is no infinite fatigue life in metallic materials. *Fatigue Fract. Eng. Mater. Struct.,* **22** (issue 7), 559-565.

8 Bathias, C., Drouillac, L., Le François, P. (2001) How and why the fatigue S–N curve does not approach a horizontal asymptote. *Int. J. Fatigue,* **23** (Supplement 1), 143–151.

9 Pyttel, B., Schwerdt, D., Berger, C. (2011) Very high cycle fatigue – Is there a fatigue limit? *Int. J. Fatigue,* **33** (Issue 1), 49-58.

10 Murakami, Y. (2002) Metal Fatigue: Effects Of Small Defects And Nonmetallic Inclusions. Elsevier Ltd, Oxford, UK.

11 Furuya, Y. (2011) Notable size effects on very high cycle fatigue properties of high strength steel. *Mater. Sci. Eng. A,* **528**, 5234–5240.

12 Paolino, D.S., Tridello, A., Chiandussi, G., Rossetto, M. (2014) On specimen design for size effect evaluation in ultrasonic gigacycle fatigue testing. *Fatigue Fract. Engng. Mater. Struct.*, **37**, 570–579.

13 Paolino, D.S., Tridello, A., Chiandussi, G. and Rossetto, M. (2016) S-N curves in the very-high-cycle fatigue regime: statistical modeling based on the hydrogen embrittlement consideration. *Fatigue Fract. Eng. Mater. Struct.*, **39**, 1319-1336.

14 Paolino, D.S., Tridello, A. (2016) Statistical Approach to the Very-High-Cycle Fatigue of Metallic Materials, *29th Symposium on Reliability Engineering and International Workshop*, Society of Material Science, Tokyo (Japan), 15-16 December 2016.

15 Jiang, Z., Dong, Y., Liang, L., Li, Z. (2011) Hydrogen Pick-Up During Electroslag Remelting Process. *J Iron Steel Res. Int.*, **18** (issue 4), 19-23.

16 Totten, G. E., Xie, L., Funatani, K. (2003) Handbook of Mechanical Alloy Design. CRC Press, New York, USA.

17 Sawahata, A., Tanigawa, H., Enomoto, M. (2008) Effects of ElectroSlag Remelting on Inclusion Formation and Impact Property of Reduced Activation Ferritic/Martensitic Steels. *J. of the Japan Institute of Metals*, **72** (3), 176-180.

18 EN ISO 6507-1 (2005) Metallic materials - Vickers hardness test - Part 1: Test method, International Standard Organization, Genève.

19 ASTM Standard E1876-09 (2009). Standard test method for dynamic Young's modulus, Shear modulus, and Poisson's ratio by impulse excitation of vibration, ASTM Standard, West Conshohocken (PA).

20 Tridello, A., Paolino, D.S., Chiandussi, G., Rossetto, M. (2016) Gaussian specimens for VHCF tests: Analytical prediction of damping effects. *Int. J. Fatigue*, **83**, 36-41.

21 Beretta, S., Anderson, C., Murakami, Y. (2006) Extreme value models for the assessment of steels containing multiple types of inclusion. *Acta Mater.*, **54**, 2277-2289.

22 Spriestersbach, D., Grad, P., Kerscher, E. (2014) Crack initiation mechanisms and threshold values of very high cycle fatigue failure of high strength steels. *Procedia Eng*, **74**, 84-91.

23 Matsunaga, H., Sun, C., Hong ,Y., Murakami, Y. (2015) Dominant factors for very-high-cycle fatigue of high-strength steels and a new design method for components. *Fatigue Fract. Engng. Mater. Struct*., **38**, 1274–1284.

24 Li, W., Deng, H., Sun, Z., Zhang, Z., Lu, L., Sakai, T. (2015) Subsurface inclusion-induced crack nucleation and growth behaviors of high strength steels under very high cycle fatigue: Characterization and microstructure-based modelling. *Mater Sci Eng A*, **641**, 10-20.

25 Hong, Y., Lei, Z., Sun, C., Zhao, A. (2014) Propensities of crack interior initiation and early growth for very-high-cycle fatigue of high strength steels. *Int. J. Fatigue*, **58**, 144-151.

26 Shiozawa, K., Lu, L., Ishihara, S. (2001) S–N curve characteristics and subsurface crack initiation behaviour in ultra-long life fatigue of a high carbon–chromium bearing steel. *Fatigue Fract. Eng. Mater. Struct*., **24**, 781–790.

27 Li, Y.D., Zhang, L.L., Fei, Y.H., Liu, X.Y. and Li, M.X. (2016) On the formation mechanisms of fine granular area (FGA) on the fracture surface for high strength steels in the VHCF regime. *Int. J. Fatigue*, **82**, 402–410.

28 Mughrabi, H. (2006) Specific features and mechanisms of fatigue in the ultrahigh-cycle regime. *Int. J. Fatigue*, **28**, 1501-1508.

29 Pineau A., Antolovich S.D. (2016) Probabilistic approaches to fatigue with special emphasis on initiation from inclusions. *Int. J. Fatigue*, **93,** 422–434.

30 Tridello, A., Paolino, D.S., Chiandussi, G., Rossetto, M. (2015) VHCF response of AISI H13 steel: assessment of size effects through Gaussian specimens, *Procedia Eng.*, **109**, 121-127.

31 Tridello, A., Paolino, D.S., Chiandussi, G., Rossetto, M. (2016) VHCF strength decrement in large H13 steel specimens subjected to ESR process, *Procedia Struct. Eng.*, **2**, 1117-1124.

32 Zhang, J.W., Lu, L.T., Wu, P.B., Ma, J.J., Wang, G.G., Zhang, W.H. (2013) Inclusion size evaluation and fatigue strength analysis of 35CrMo alloy railway axle steel, *Mater. Sci. Eng. A*, **562**, 211-217
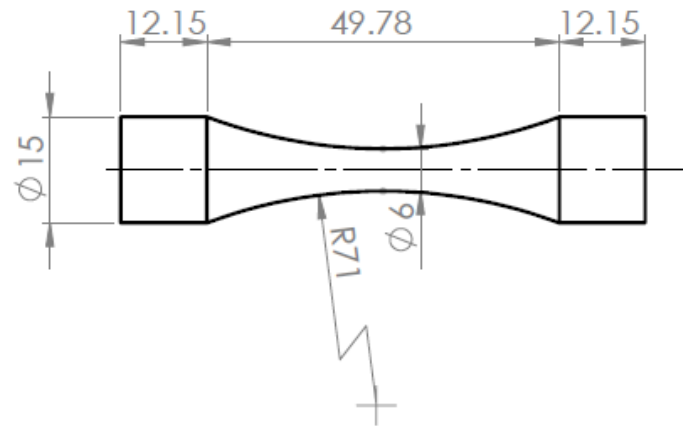
Figure captions

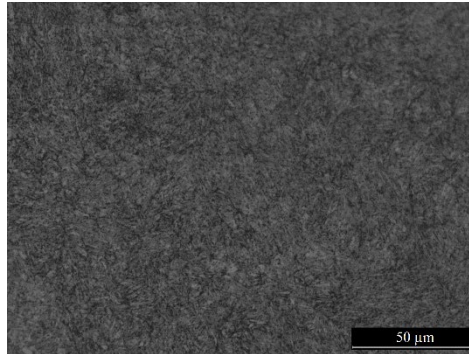Figure 1: Geometry of the hourglass specimen.

Figure 2: Tempered martensite microstructure obtained after the heat treatment (H13-ESR steel).

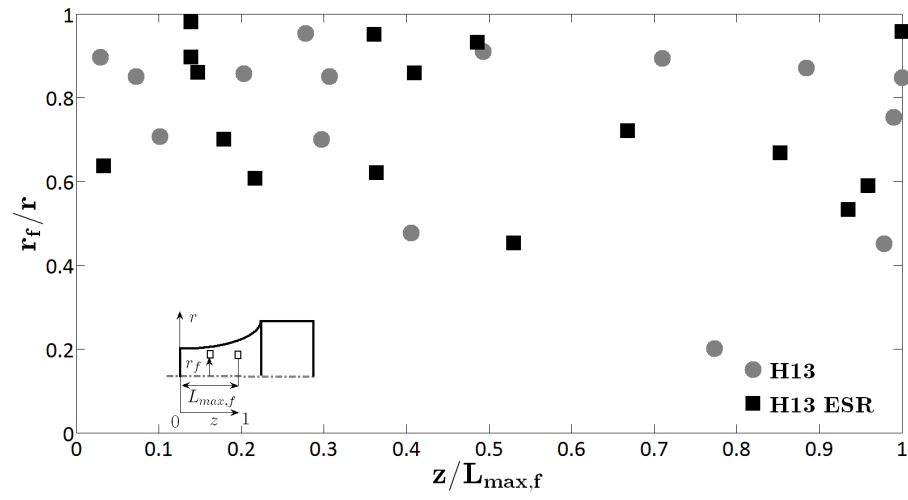Figure 3: Typical setup in an ultrasonic VHCF test.

Figure 4: Distribution of failures within the specimen risk-volume: failure location in the radial direction vs. failure location in the axial direction.
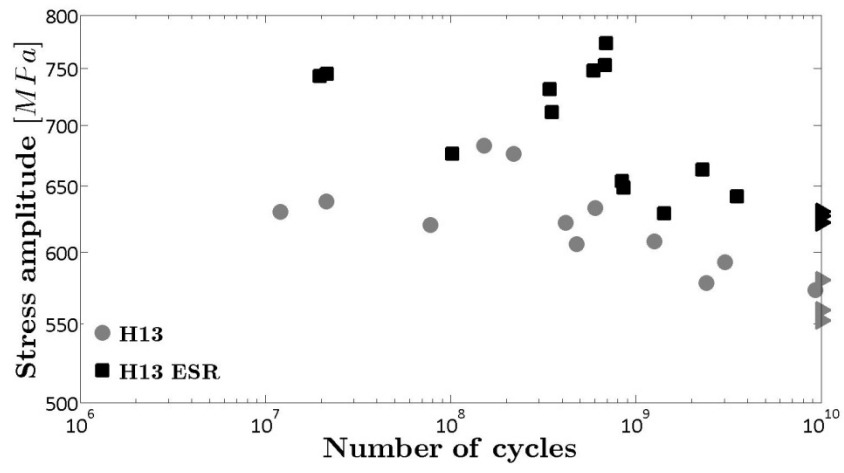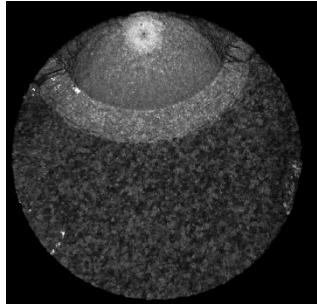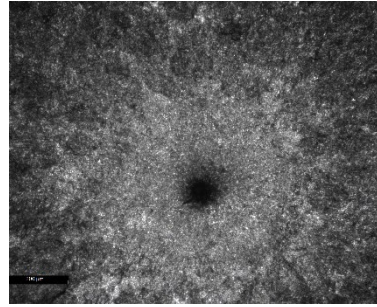
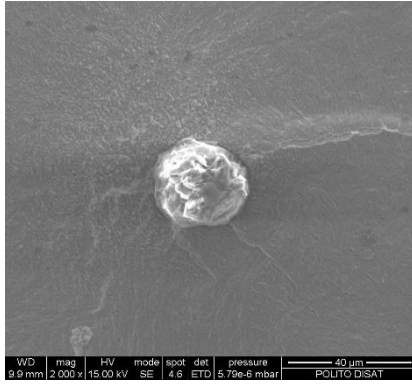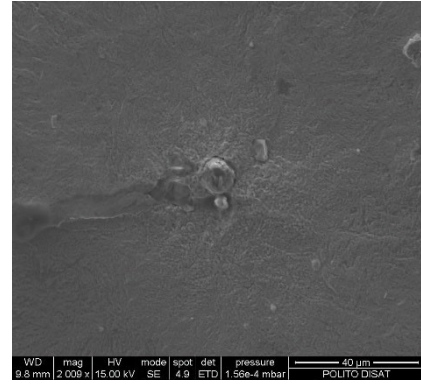Figure 5: S-N plot of the experimental results computed by considering the local stress amplitude, σ_{local}.

Figure 6: Fish-eye fracture found experimentally: a) fish-eye morphology; b) enlargement of the ODA.

Figure 7: Different types of initial defect: (a) single spherical inclusion (H13; $\sigma_{local} = 608$ MPa; $N_f = 1.25 \cdot 10^9$); (b) cluster of small inclusions (H13-ESR; $\sigma_{local} = 629$ MPa; $N_f = 1.42 \cdot 10^9$).

Figure 8: Gumbel plot of the inclusion size for the investigated steels.

Fig. 9: SIF threshold with respect to $\sqrt{a_{ODA}}$ for the investigated steels.

Figure 10: SIF threshold with respect to the number of cycles to failure for the investigated steels.

Figure 11: Median fatigue limit curve for the H13 and the H13-ESR steel.

Figure 12: P-S-N curves for an initial defect with median size.

Figure 13: Marginal 1% P-S-N curves for the two investigated steels.

Figure 14: Median fatigue limit design curves for the two investigated steels: $\sigma_{l,H}$ and $\sigma_{l,G}$ denote predicted and experimental[12,13] values at $V_{90} = 2300 \text{ mm}^3$.

Figure 15: Proposed design methodology based on the *fatigue limit design curve.*

Figure 1: Geometry of the hourglass specimen.

Figure 2: Tempered martensite microstructure obtained after the heat treatment (H13-ESR steel).

Figure 3: Typical setup in an ultrasonic VHCF test.

Figure 4: Distribution of failures within the specimen risk-volume: failure location in the radial direction vs. failure location in the axial direction.

Figure 5: S-N plot of the experimental results computed by considering the local stress amplitude, σ_{local}.

(a)   (b)

Figure 6: Fish-eye fracture found experimentally: a) fish-eye morphology; b) enlargement of the ODA.

Figure 7: Different types of initial defect: (a) single spherical inclusion (H13; $\sigma_{local} = 608$ MPa; $N_f = 1.25 \cdot 10^9$); (b) cluster of small inclusions (H13-ESR; $\sigma_{local} = 629$ MPa; $N_f = 1.42 \cdot 10^9$).

Figure 8: Gumbel plot of the inclusion size for the investigated steels.

Fig. 9: SIF threshold with respect to $\sqrt{a_{ODA}}$ for the investigated steels.

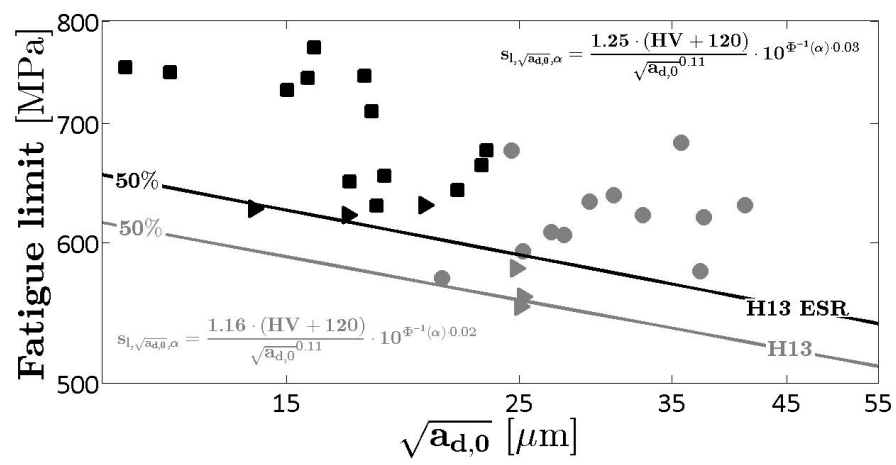Figure 10: SIF threshold with respect to the number of cycles to failure for the investigated steels.

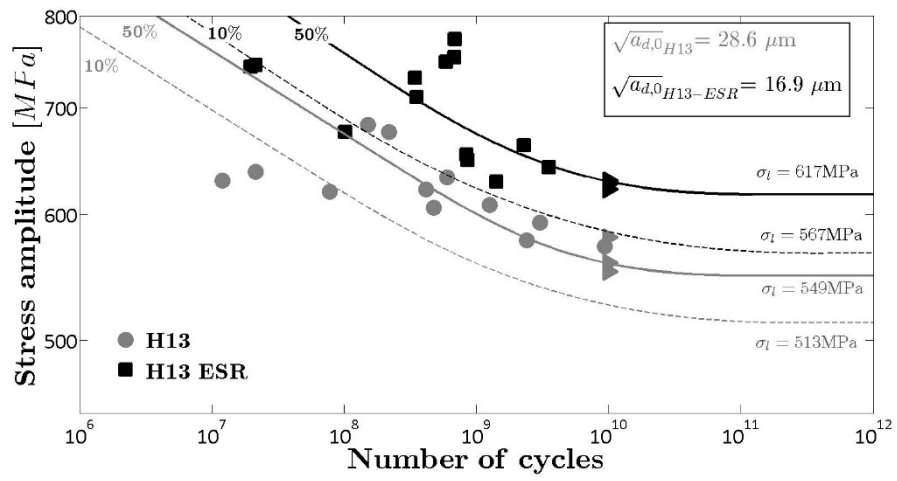Figure 11: Median fatigue limit curve for the H13 and the H13-ESR steel.

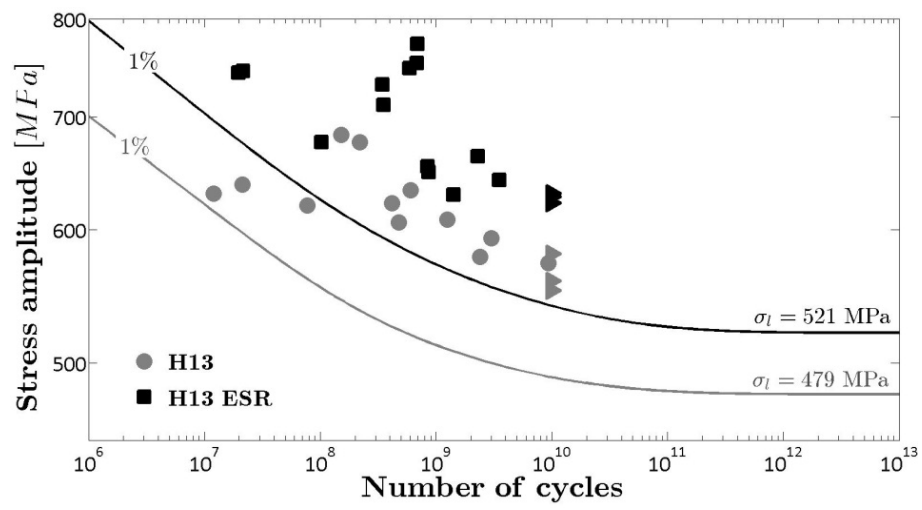Figure 12: P-S-N curves for an initial defect with median size.

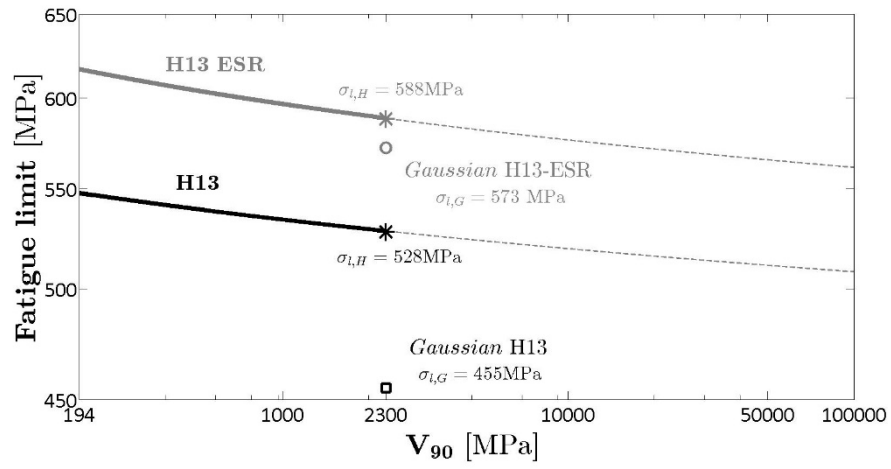Figure 13: Marginal 1% P-S-N curves for the two investigated steels.

Figure 14: Median fatigue limit design curves for the two investigated steels: $\sigma_{l,H}$ and $\sigma_{l,G}$ denote predicted and experimental[12,13] values at $V_{90} = 2300 \text{ mm}^3$.
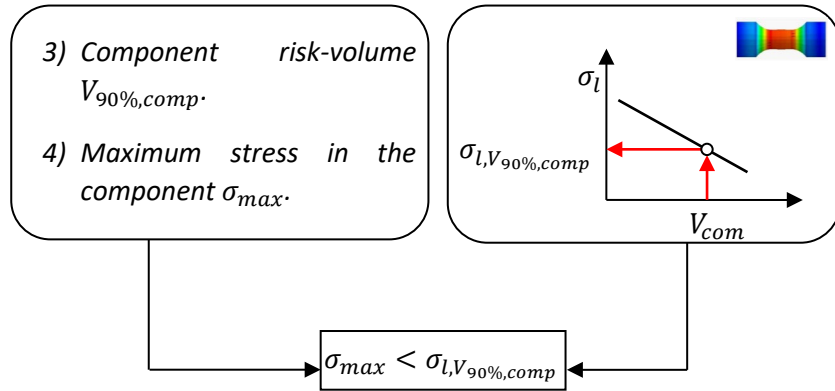
Figure 15: Proposed design methodology based on the *fatigue limit design curve.*

Table captions

Table 1: Chemical composition of the AISI H13 steel.

Table 2: Materials properties experimentally determined.

Table 3: Summary of the experimental results.

Table 1: Chemical composition of the AISI H13 steel.

Element	C	Si	Mn	Cr	Mo	V
%	0.39	1	0.4	0.4	5.3	0.9

Table 2: Mechanical properties of the investigated steels.

Material	σ_u [MPa]	E_d [GPa]	HV [HV]
H13	2000	212	560
H13-ESR	2100	213	560

Table 3: Summary of the experimental results.

Material	Number of specimens	Stress range [MPa]	Number of runouts	Minimum N_f	Maximum N_f
H13	15	$[570 - 710]$	3	$4.5 \cdot 10^6$	$9.4 \cdot 10^9$
H13-ESR	16	$[630 - 810]$	3	$2.0 \cdot 10^7$	$3.5 \cdot 10^9$